

# Tuning Point Defects by Elastic Strain Modulates Nanoparticle Exsolution on Perovskite Oxides

Jiayue Wang, Jing Yang, Alexander K. Opitz, William Bowman, Roland Bliem, Georgios Dimitrakopoulos, Andreas Nenning, Iradwikanari Waluyo, Adrian Hunt, Jean-Jacques Gallet, and Bilge Yildiz\*



Cite This: <https://doi.org/10.1021/acs.chemmater.1c00821>



Read Online

ACCESS |



Metrics & More

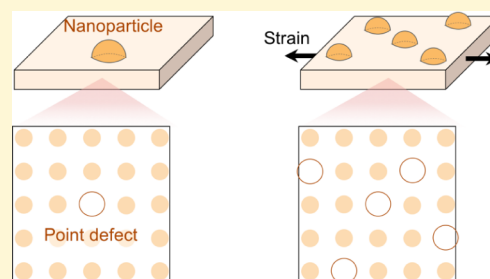


Article Recommendations



Supporting Information

**ABSTRACT:** Exsolution generates stable and catalytically active metal nanoparticles via phase precipitation out of a host oxide. An ability to control the size and dispersion of the exsolution particles is desirable for design of nanostructured (electro)catalysts. Here, we demonstrate that tuning point defects by lattice strain affects both the thermodynamics and the kinetics of iron ( $\text{Fe}^0$ ) exsolution on  $\text{La}_{0.6}\text{Sr}_{0.4}\text{FeO}_3$  (LSF) thin film model. By combining *in situ* surface characterization and *ab initio* defect modeling, we show oxygen vacancy and Schottky defects to be the primary point defects formed upon  $\text{Fe}^0$  exsolution. Lattice strain tunes the formation energy, and thus the abundance of these defects, and alters the amount and size of the resulting exsolution particles. In addition, we find that the density of exsolved nanoparticles matches the concentration of oxygen vacancy pairs, thus pointing to the surface oxygen vacancy pairs as preferential nucleation sites for exsolution. The tensile-strained LSF with a facile formation of these critical point defects results in a higher  $\text{Fe}^0$  metal concentration, a larger density of nanoparticles, and a reduced particle size at its surfaces. These results provide important mechanistic insights and highlight the role of point-defect engineering in designing nanostructured catalysts in energy and fuel conversion technologies.



## INTRODUCTION

Oxide-supported metal nanoparticles are key functional components in a wide range of energy storage and conversion technologies.<sup>1–3</sup> A recent advance in the design of materials for these applications is to *exsolve* metal nanoparticles that act as catalysts for reactions of interest. In this process, catalytically active transition metals are first substituted into the parent oxide under oxidizing conditions, and the metallic nanoparticles are then precipitated from the host matrix upon reduction. Nishihata et al. initially demonstrated exsolution in three-way catalysts.<sup>4</sup> Compared to particles prepared by deposition or impregnation,<sup>1,5</sup> the exsolved nanoparticles are partially embedded in the parent oxide.<sup>6</sup> Their anchored structure makes the exsolved nanoparticles highly resistant toward coarsening<sup>7,8</sup> and helps maintain the particles in their original position of nucleation.<sup>9</sup> In addition, the exsolved particles are more resilient against coking<sup>6</sup> and can be redissolved into the host oxide upon oxidation at elevated temperatures for catalyst regeneration.<sup>10,11</sup> Today, the concept of exsolution has been expanded to a number of other applications including solid oxide electrochemical cells,<sup>12–14</sup> ceramic membrane reactors,<sup>15,16</sup> chemical looping combustion,<sup>17</sup> and photocatalysis.<sup>18</sup> Due to the size-dependent performance of supported metal catalysts,<sup>19</sup> exsolved nanoparticles with ever smaller sizes and higher densities are desirable. Since exsolution often requires long-time reduction at elevated temperatures, some coarsening of particles seems to

be inevitable.<sup>8,20–22</sup> As a result, the current exsolution studies typically report metal nanoparticles with tens of nanometers in size. To establish a desired morphology of the exsolved nanoparticles, one has to be able to control the exsolution parameters, through the underlying mechanisms.

Herein, we propose that an ability to control the point defect formation in the host oxide is needed to tune exsolution, both thermodynamically and kinetically. First, formation of oxygen vacancy and cation vacancy defects has been suggested as the elementary processes in exsolution.<sup>23,24</sup> Thus, the ease to form these defects in the host oxide is a key factor in the thermodynamics as well as the kinetics of exsolution. As an example, an increased concentration of A-site vacancies and oxygen vacancies in perovskite oxides ( $\text{ABO}_3$ ) has been observed to assist B-site exsolution by creating local B-site excess<sup>25</sup> and under-coordinated B-site cations,<sup>23,26</sup> respectively. Second, it is known that oxygen vacancies on oxide surfaces can serve as preferential nucleation sites for supported metal nanoparticles, based on the increased binding energy of metal atom clusters to such point defects.<sup>27,28</sup> Using the same

Received: March 8, 2021

Revised: May 26, 2021



ACS Publications

© XXXX American Chemical Society

A

<https://doi.org/10.1021/acs.chemmater.1c00821>  
Chem. Mater. XXXX, XXX, XXX–XXX

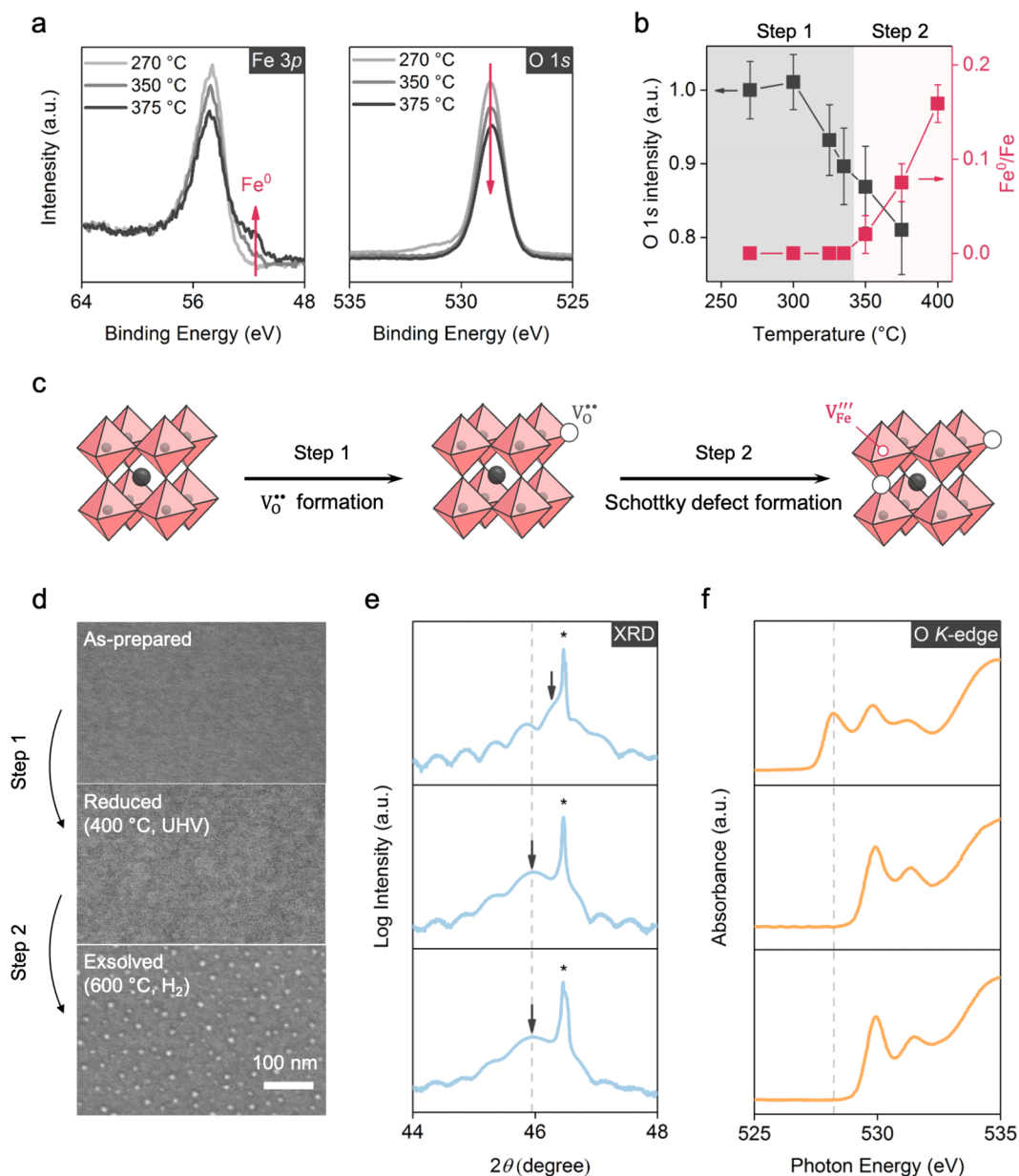


**Figure 1.** Chemistry and structure of LSF prior to and upon exsolution. (a) Fe 3p and O 1s spectra collected *in situ* in 0.5 Torr H<sub>2</sub> under different temperatures. Fe 3p and O 1s spectra were collected at a photon energy of 420 and 860 eV, respectively. (b) Evolution of surface Fe<sup>0</sup> concentration and the normalized O 1s intensity during exsolution. (c) Schematic representation of the point defect formation reactions in LSF during exsolution: first formation of oxygen vacancies, followed by the Schottky defects. (d) SEM images, (e) out-of-plane symmetric  $2\theta$ - $\omega$  XRD patterns, and (f) O K-edge TEY-XAS measurement of the as-prepared (top), reduced (middle), and exsolved (bottom) LSF. The XRD scan is collected at the pseudocubic (002) reflection, where LSF and SrTiO<sub>3</sub> substrate peaks are indicated with an arrow and an asterisk, respectively.

argument, we propose that oxygen vacancies can also increase the nucleation density and rate of exsolution of particles and, hence, increase the nanoparticle density and dispersion.<sup>29</sup>

Establishing the connection between the microscopic point defect formation and the macroscopic nanoparticle exsolution, however, is not trivial. The first challenge is to isolate point defect formation from other experimental parameters. Most studies, to date, focused on screening different host perovskite oxides and different metal cation dopants to examine the exsolution process as a function of defect concentration.<sup>23,25</sup> However, the large variety in the surveyed compositions introduces the uncertainty that other factors may interfere, for example, the difference in the solubility of a given metal in

different perovskite hosts.<sup>30,31</sup> This complexity requires a method to decouple point defect formation during reduction, from other compositional effects on exsolution. Keeping the cation composition fixed while altering the concentration and stability of point defects in the host oxide by external fields is desirable for this purpose. The second challenge is to identify the key defect structure that facilitates the nucleation of exsolving particles. Previous studies have calculated the B-site segregation energy (as a metric for exsolution) as a function of defect concentration.<sup>23,32–34</sup> However, it remains unclear how the point defect type, structure, and distribution affect the particle nucleation process in exsolution. As noted above, oxygen vacancies may play a role here, akin to their role in

binding the supported metal nanoparticles.<sup>27,28</sup> To address this problem, one needs to develop a method to link the local point defect chemistry and structure to the exsolution properties of the host oxide.

In this work, we present an experimental and analysis framework to tackle both of the challenges noted above. We use biaxial lattice strain as an approach to tailor point defect formation without changing the nominal cation composition of the host oxide. Previous studies have shown that lattice strain can change the concentration,<sup>35,36</sup> migration barrier,<sup>37</sup> as well as the degree of ordering<sup>38</sup> of point defects in oxides. Therefore, by tuning the formation energy (and thus the abundance) of the point defects in the host oxide with biaxial lattice strain, we can examine their impact on metallic nanoparticle exsolution while keeping the nominal composition of the perovskite unchanged. To quantitatively interpret the role of point defects, we developed a multiscale defect model by combining density functional theory (DFT) calculations and Monte Carlo (MC) simulations. We used the former to obtain the energetics associated with strain-dependent point defect formation, as well as binding of metal atoms to point defects, and the latter to identify the critical defect structures that facilitate nanoparticle nucleation.

To demonstrate this approach, we take epitaxial  $\text{La}_{0.6}\text{Sr}_{0.4}\text{FeO}_3$  (LSF) thin films as a model system, primarily due to its well-studied defect chemistry and the range of applications that use it as an electrocatalyst.<sup>39,40</sup> Previous studies have demonstrated that upon reduction (both chemically<sup>22,41</sup> and electrochemically,<sup>42–44</sup> metallic iron particles ( $\text{Fe}^0$ ) can be exsolved from the LSF lattice. It is known that exsolution can occur both at the surface and in the bulk of an oxide.<sup>45,46</sup> Recently, *in situ* transmission electron microscopy experiments have demonstrated that the metal nanoparticles nucleate directly at the surface of a perovskite oxide at early stages of exsolution.<sup>9,17</sup> Since the nanoparticles being exsolved on the surface are of greater importance for catalysis and electrocatalysis, we focus on the surface exsolution on LSF in this work.

By quantifying surface defect states with near-ambient pressure X-ray photoelectron spectroscopy (NAP-XPS), we identify the initial oxygen vacancy formation and the following Schottky defect formation as the primary defect reactions prior to and during  $\text{Fe}^0$  nanoparticle exsolution on LSF. MC simulations, using *ab initio* defect and binding energies, show that oxygen vacancy pair concentration at the surface correlates well with the experimentally found nanoparticle concentration, and thus, these defect pairs could serve as nucleation sites for the exsolved  $\text{Fe}^0$  nanoparticles. DFT calculations also confirm the oxygen vacancy pairs to be a more favorable binding site for Fe adatoms and Fe dimers, compared to isolated oxygen vacancy. Then, by tuning the formation of oxygen vacancy and Schottky defects in the LSF thin films with lattice strain, while keeping all other experimental parameters unchanged, we unequivocally demonstrate the capability to tailor nanoparticle exsolution via point defect control. As a result, the LSF surface with the most enhanced point defect formation under tensile strain had the highest  $\text{Fe}^0$  concentration, the largest particle density, as well as the finest particle size. The strain-modified point defect formation model here can also reconcile the inconsistent strain dependencies that have been reported for exsolution on different perovskite oxides (discussed below).<sup>47,48</sup> Our results highlight the fundamental role of

point defects in tailoring exsolution and engineering nanostructured catalysts.

## ■ RESULTS AND DISCUSSION

**Point Defect Reactions Prior to and at the Onset of Exsolution.** We assessed the surface defect chemistry during exsolution on the LSF film grown on  $\text{SrTiO}_3(001)$  substrate using NAP-XPS. The LSF thin film was heated in 0.5 mbar of dry  $\text{H}_2$  during continuous gas flow (Supplementary Note 1). As shown in Figure 1a, a feature at 51.5 eV in the Fe 3p spectra emerges at 350 °C, which can be assigned to the metallic  $\text{Fe}^0$  species (Supplementary Note 2). The intensity of this  $\text{Fe}^0$  species indicates the amount of Fe exsolution. Meanwhile, two changes in the normalized O 1s spectra arise during Fe exsolution. First, the overall intensity of the normalized O 1s spectra decreased upon heating in  $\text{H}_2$  atmosphere, indicating an increase in the oxygen nonstoichiometry ( $\delta$  in  $\text{La}_{0.6}\text{Sr}_{0.4}\text{O}_{3-\delta}$ ) in the near-surface region.<sup>49</sup> (XPS analysis approach is presented in Supplementary Note 3.) Second, when the LSF surface is being reduced, the oxygen species at ~532 eV, which is usually assigned to the segregated SrO surface layer of the perovskite,<sup>50,51</sup> vanishes. A consistent observation regarding the disappearance of the surface Sr species is present in the Sr 3d spectra (Supplementary Note 4).

The evolution of the surface  $\text{Fe}^0$  concentration, along with the relative change in the normalized O 1s intensity, is plotted in Figure 1b, as a function of the reduction temperature. As illustrated, the surface chemical evolution during the exsolution process consists of two stages. First, when heating the sample in  $\text{H}_2$  at a temperature below 350 °C, the surface became more reduced as is featured by a decrease in the O 1s intensity, consistent with the formation of oxygen vacancies near the surface. Meanwhile, no  $\text{Fe}^0$  was present on the surface. In the second stage, when the reduction temperature is higher than 350 °C,  $\text{Fe}^0$  appeared at the surface, and its concentration increase was accompanied by a further decrease in the O 1s intensity. The absolute values of the O 1s intensity change in Figure 1b should be treated as only semiquantitative. This is because exsolution introduces chemical and roughness evolution on the surface, making it very difficult to find a constant surface species to normalize the O 1s spectra. Nevertheless, the quantification uncertainties do not impede the demonstration of the increase in the oxygen nonstoichiometry during exsolution.

Based on the NAP-XPS results, we show Fe metal precipitation can only occur beyond a certain threshold of reduction. We can thus ascribe two types of point defect reactions being involved in the exsolution process (schematically shown in Figure 1c). In the first step, which we call mild reduction, the oxidized perovskite releases lattice oxygen (seen as the decrease in O 1s signal), forming oxygen vacancies, without reaching its critical decomposition nonstoichiometry. This step is prior to metal precipitation and can be expressed in Kröger–Vink notation<sup>52</sup> as



where  $\text{O}_\text{O}^\times$ ,  $\text{V}_\text{O}^{\bullet\bullet}$ ,  $\text{e}'$ , and  $\text{O}_\text{atm}$  denote a neutral lattice oxygen, a doubly positive-charged oxygen vacancy, an electron, and an oxygen atom in the gas phase, respectively. Depending on the reducing agent,  $\text{O}_\text{atm}$  can be present in the form of different molecules such as  $\text{O}_2$ ,  $\text{H}_2\text{O}$ , and  $\text{CO}_2$ .

In the second step, which involves metal phase precipitation, metallic Fe species form together with the oxygen release (as



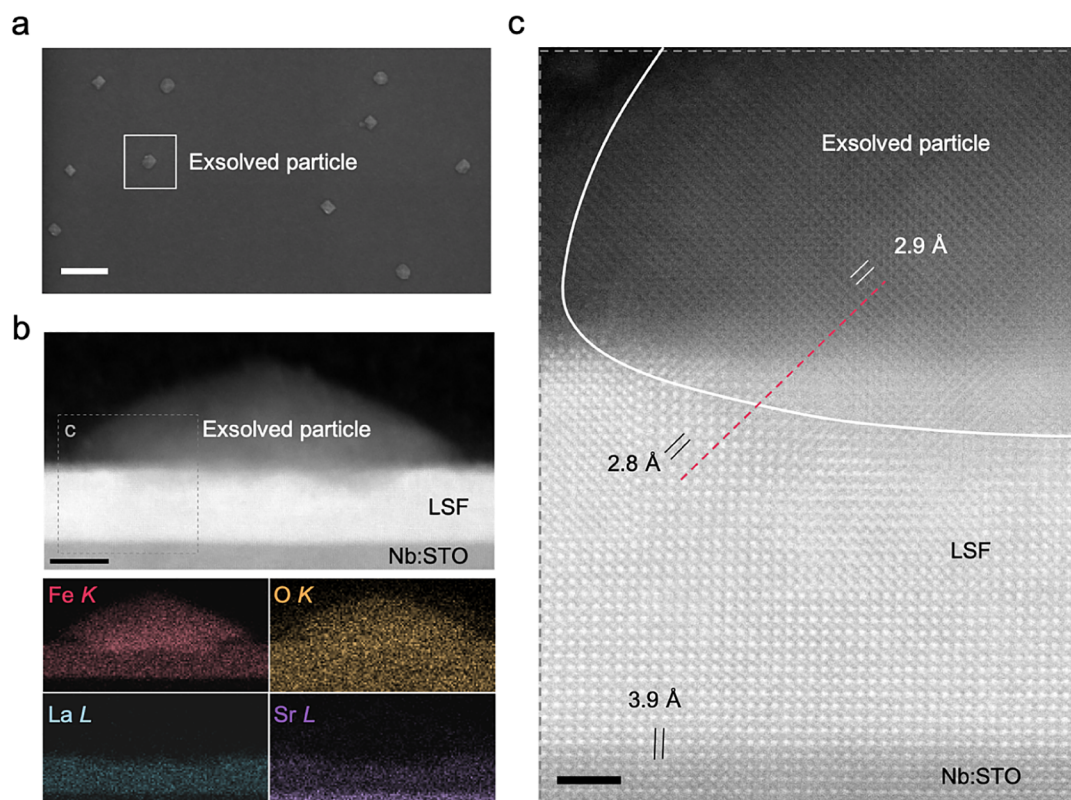
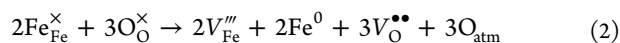


**Figure 2.** Atomic structure and chemical nature of the exsolved nanoparticles. (a) SEM image (scale bar: 200 nm) of an LSF film after being reduced in 200 sccm 3%  $\text{H}_2/\text{N}_2$  at 650 °C for 5 h. (b) Low magnification high-angle annular dark field (HAADF) STEM cross-sectional image (scale bar: 10 nm) of the same sample as in (a), together with the corresponding elemental maps obtained by EDX. (c) High-resolution HAADF image (scale bar: 2 nm) of the region highlighted in (b). Note that the exsolved particle is partially embedded in the LSF thin film and forms a coherent particle/oxide interface.

revealed by the NAP-XPS measurement in Figure 1b). Upon sufficient reduction, this leads to the nucleation of metal nanoparticles. This step is associated with oxygen release and metal precipitation, resulting in the formation of  $2V_{\text{Fe}}''' - 3V_{\text{O}}'' + 3\text{O}_{\text{atm}}$  Schottky defects within the lattice



where  $\text{Fe}_{\text{Fe}}^{\times}$ ,  $V_{\text{Fe}}'''$ , and  $\text{Fe}^0$  denote a neutral Fe site, a triply negatively charged Fe vacancy, and Fe metal species, respectively. We recognize that Schottky defects can include A-site vacancies as well, but we do not have evidence to these defects that would result in the formation of La or Sr precipitation under these conditions. As presented in Figure S6, the La 4d and Sr 3d XPS spectra remained unchanged during the experiment. As such, we only considered Fe and O vacancies as a part of the Schottky defect formation process. Meanwhile, we are aware that several intermediate steps may take place in exsolution so that  $\text{Fe}^0$  does not necessarily form directly from  $\text{Fe}^{3+}$ . For example,  $\text{Fe}^{3+}$  can be first reduced into  $\text{Fe}^{2+}$  and precipitate as iron oxide prior to  $\text{Fe}^0$  formation. Nevertheless, since the goal of eq 2 is to describe the overall thermodynamic driving force instead of microkinetics, we keep the current format for clarity and simplicity.

We further demonstrate the role of these two defect reactions in exsolution, with a coupled chemical, morphological, and structural characterization of the LSF thin film. To begin with, we reduce the LSF film at 400 °C in ultrahigh vacuum (UHV) to mildly reduce the sample. As illustrated in Figure 1d–f, although no particles appeared on the surface

during the mild reduction step, the out-of-plane lattice parameter increased by 0.6% ( $\pm 0.1\%$ ) compared to the as-prepared one. This chemical expansion is induced by oxygen vacancy formation,<sup>53</sup> and similar lattice expansion as a result of oxygen release has also been reported for LSF powders.<sup>54</sup> According to the bulk chemical expansion coefficient,<sup>40</sup> the 0.6% lattice expansion corresponds to an increase of 0.3 in  $\delta$  prior to the onset of exsolution (Supplementary Note 3). While a quantitative comparison between NAP-XPS and XRD is not possible due to the different probing depths and experimental conditions, both techniques consistently point to the increase in  $\delta$  in the LSF lattice during the prerelation step. The formation of oxygen vacancies during this step is also confirmed by total electron yield mode X-ray absorption spectroscopy (TEY-XAS). In the as-prepared LSF, the pre-edge band is clearly visible in the O K-edge (Figure 1f). This feature is assigned to an empty state in the oxygen–iron molecular orbital—i.e., the electron hole charge compensating the Sr doping.<sup>55</sup> Upon reduction, the pre-edge feature completely vanishes, indicating that the hole concentration becomes negligible due to the increased oxygen deficiency in LSF.<sup>40</sup>

During the second step, involving more significant reduction after heating the sample to 600 °C in 80 mTorr  $\text{H}_2$ , the particles started to appear on the surface, as seen in Figure 1d. Since there is metal precipitation at this step, this has to be associated with Schottky defect formation within the lattice (eq 2). Nevertheless, no apparent lattice volume change could be detected with the XRD measurement during this step, as

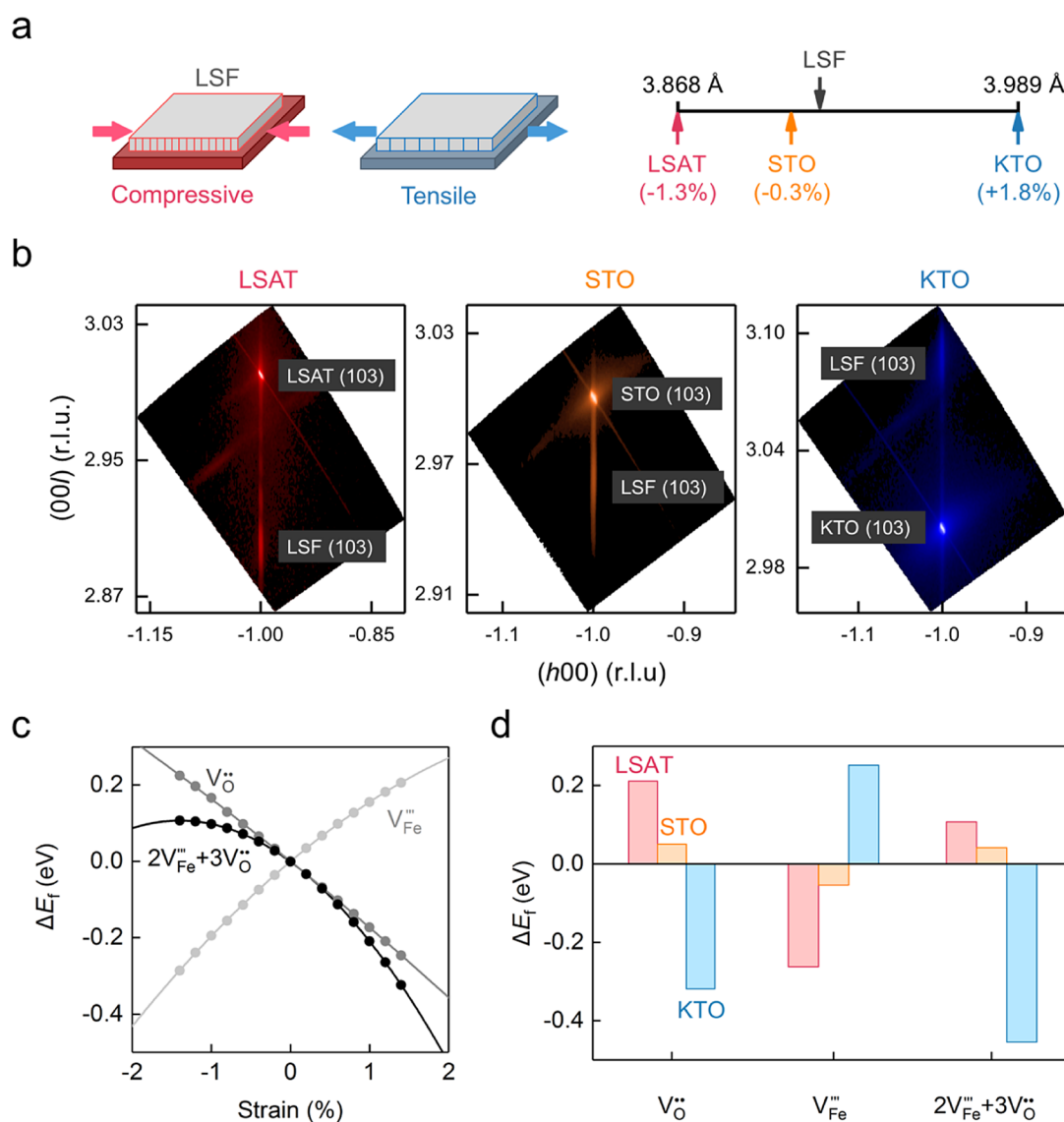


**Figure 3.** Tuning point defect formation in the LSF thin films with biaxial lattice strain. (a) Schematic representation depicting the sample geometry, where biaxial lattice strain is introduced by heteroepitaxy. The number of lines indicates the range of in-plane strains achieved in LSF. Here, the tensile strain is denoted as positive, and compressive strain as negative. (b) X-ray RSM about the (103) reflection of coherently strained LSF thin films, collected after the exsolution test. Note the film peaks are directly below or above that of the substrate, confirming identical in-plane lattice constants and that the epitaxy is preserved after this exsolution process. (c) Change in the defect formation energy for the oxygen vacancy, iron vacancy, and the Schottky defect versus biaxial lattice strain. The data points are calculated by DFT, while the lines represent the parabolic fits. The zero reference point corresponds to the unstrained state. Note that tensile strain facilitates the formation of both the oxygen vacancy and the Schottky defect. (d) Calculated defect formation energy difference at the nominal strain values of the differently strained LSF films. The unit cell used in the DFT calculation is described in Supplementary Note 7.

indicated by the dashed line in Figure 1e. This may arise from two possible scenarios: counteraction of cation and anion vacancy formation on the lattice volume, as cation vacancies contract the lattice while oxygen vacancies expand it;<sup>56,57</sup> and a nonuniform distribution of Schottky defects that is confined to the near-surface region under diffusion-limited conditions (Supplementary Note 5). In addition, we did not observe diffraction peaks for metallic iron and  $\text{LaSrFeO}_4$  in the exsolved LSF film—the two characteristic phases for fully decomposed LSF thin films.<sup>58,59</sup> These observations indicate that the LSF films investigated in this work were at early stages of surface exsolution, prior to bulk metal precipitation (decomposition).<sup>60</sup>

The structure and chemical composition of the exsolved nanoparticles were further investigated by aberration-corrected scanning transmission electron microscopy (STEM) imaging and energy-dispersive X-ray spectroscopy (EDX). To facilitate the STEM specimen preparation, large exsolved nanoparticles are needed, and so the LSF film was exsolved in a harsh reducing environment (3%  $\text{H}_2/\text{N}_2$ , 650 °C, see Methods for details) prior to STEM. As a result, the nanoparticles in the STEM imaging were larger than the other nanoparticles presented in this work, which were imaged right after the exsolution onset. The planar and cross-sectional views of the exsolved LSF film are presented in Figure 2a,b, respectively. While exsolution can occur both at the surface and in the bulk of the host oxide,<sup>45,46</sup> only surface exsolution was observed in

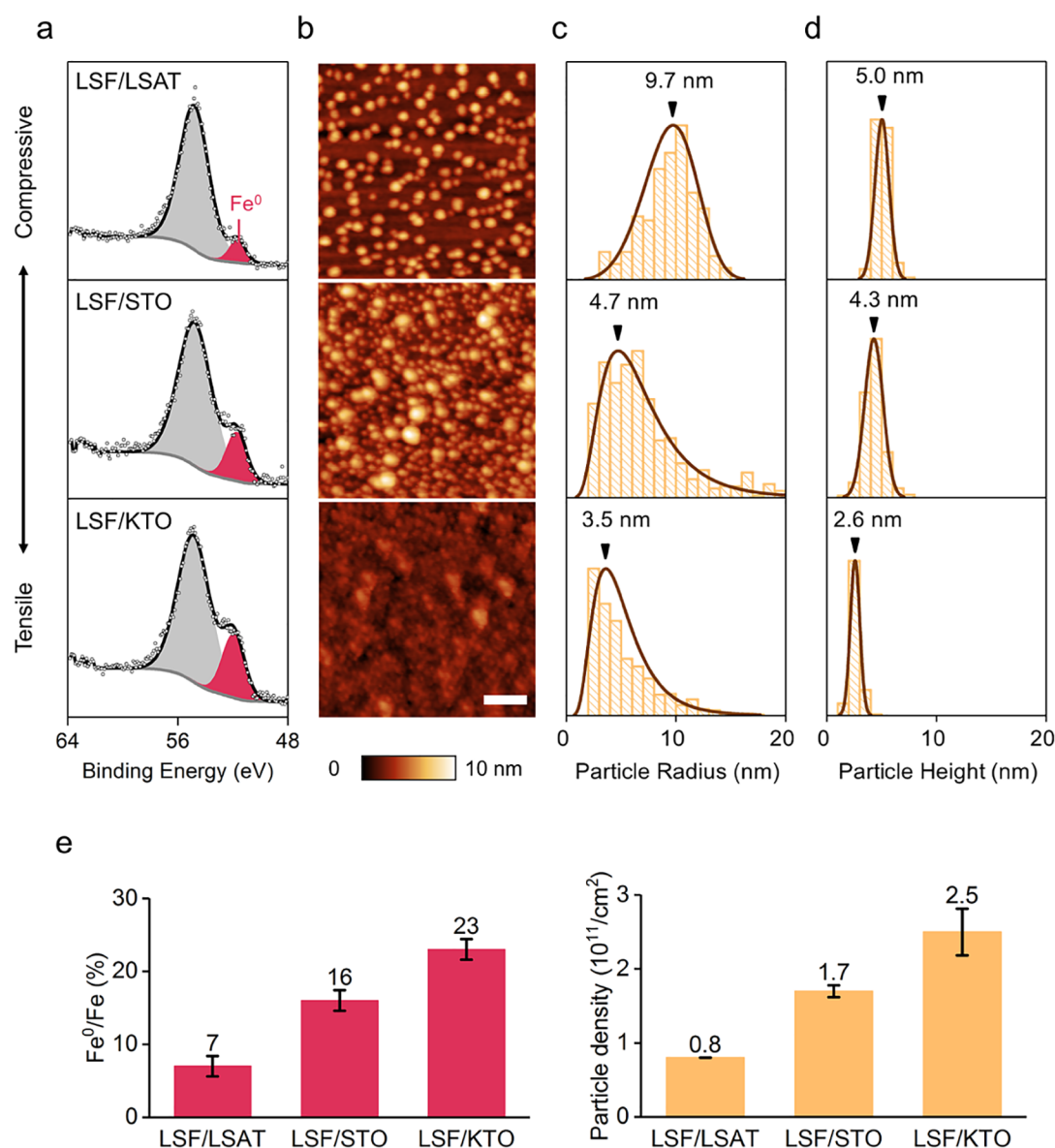


**Figure 4.** Comparison of Fe<sup>0</sup> exsolution on the LSF thin films with strain-modulated point defect formation. (a) Comparison of *in situ* Fe 3p spectra at 400 °C in 0.5 mbar H<sub>2</sub>, where the LSF film under tensile strain (LSF/KTO) demonstrated the largest Fe<sup>0</sup> feature. (b) *Ex situ* AFM images showing the surface morphology after exsolution (scale bar: 100 nm), together with histograms of the (c) equivalent disk radius and (d) average height of the nanoparticles on the surface. From in-plane compression to tension, there is a clear decrease in both height and radius of the surface particles. (e) Surface Fe<sup>0</sup> concentration and particle density on the differently strained LSF thin films after exsolution. LSF films under tensile strain demonstrated the highest particle density as well as the largest [Fe<sup>0</sup>] at the surface upon exsolution.

this study. Assuming that the Fe vacancies are uniformly distributed in the entire film, the nanoparticles shown in Figure 2a correspond to only about ~1% Fe vacancy in LSF. In addition, the particles are partially embedded into the LSF surface. As discussed in the Introduction section, this “anchored” structure is a typical characteristic of exsolved nanoparticles.<sup>6</sup> The elemental mapping reveals that the surface nanoparticle is composed of Fe and O. Remarkably, as indicated by the red dashed line in Figure 2c, the exsolved nanoparticle formed a coherent interface with its parent oxide. The highlighted atomic spacing of the particle represents the *d*-spacing of the (220) planes of Fe<sub>3</sub>O<sub>4</sub> (space group *Fd* $\bar{3}$ *m*), which demonstrates the (220)<sub>LSF</sub>//(220)<sub>Fe<sub>3</sub>O<sub>4</sub></sub> crystalline orientation relation at the interface. Based on the *in situ* NAP-XPS characterization (Figure 1) and thermodynamics

analysis (Supplementary Note 1), we expect the surface nanoparticles to be initially exsolved as metallic iron nanoparticles. However, the surface particles were oxidized<sup>41</sup> in air during the STEM sample preparation, which explains the iron oxide observed in the STEM characterization instead of metallic iron. This observation highlights the importance of employing *in situ* characterization tools such as NAP-XPS to investigate the exsolution process.

**Tuning Exsolution with Strain-Modified Point Defect Formation.** The abovementioned results demonstrate that V<sub>O</sub><sup>••</sup> and Schottky defect formations are the two primary point defect reactions (eqs 1 and 2, which take place prior to and during exsolution, respectively). As a result, the ease to form these two defects in the oxide lattice thermodynamically determines the onset of exsolution. In this section, we demonstrate the capability to tailor Fe<sup>0</sup> exsolution on LSF by



tuning the formation energy of these two defects with a biaxial lattice strain.

As sketched in Figure 3a, the lattice strain is introduced by growing the LSF films epitaxially onto the three (001)-oriented perovskite-type single crystal substrates with different lattice parameters:  $\text{La}_{0.18}\text{Sr}_{0.82}\text{Al}_{0.59}\text{Ta}_{0.41}\text{O}_3$  (LSAT),  $\text{SrTiO}_3$  (STO), and  $\text{KTaO}_3$  (KTO). These three LSF films are denoted with LSF/LSAT, LSF/STO, and LSF/KTO, respectively. The in-plane lattice strain  $\varepsilon$  of the LSF films is defined as

$$\varepsilon = \frac{\Delta a}{a_0} \quad (3)$$

where  $a_0$  represents the strain-free lattice parameter, and  $\Delta a$  indicates the change in lattice parameter due to substrate clamping. To verify the film epitaxy during the exsolution experiment, X-ray diffraction reciprocal space maps (RSMs) were collected after Fe exsolution. As depicted in Figure 3b, the film peaks are directly below or above that of the substrate, meaning that the LSF thin films maintained identical in-plane lattice parameters as that of the substrates even after exsolution. The RSM measurement, thus, verifies that the LSF films were coherently strained during the entire exsolution process. As discussed in Supplementary Note 6, the strains introduced by lattice clamping (eq 3) are much larger than the thermal strains during exsolution. As a result, the overall elastic strain for the three samples at the exsolution condition (400 °C) is expected to be  $-1.34\%$  (LSF/LSAT),  $-0.34\%$  (LSF/STO), and  $+1.66\%$  (LSF/KTO). Therefore, the three samples used in this work clearly represent the LSF films with three different strain states during exsolution: compressive, nearly stress-free, and tensile for LSF/LSAT, LSF/STO, and LSF/KTO, respectively.

To illustrate how the point defect formation energy in LSF is modulated by the biaxial lattice strain, we used DFT to calculate the defect formation energy in LSF as a function of lattice strain. A slightly different composition ( $\text{La}_{0.5}\text{Sr}_{0.5}\text{FeO}_3$ ) was chosen in the DFT calculation to reduce the size of the simulation cell and minimize the calculation time needed. Consistent with experimental samples, the cell is strained in-plane and fully relaxed in the out-of-plane direction (Supplementary Note 7). As a result of these calculations, we find that oxygen vacancy formation in the  $2 \times 2 \times 2$  LSF unit cell expands the lattice by  $\sim 2\%$ , while an Fe vacancy alone contracts the lattice by  $\sim 2\%$ . Consistent with their volume change, the formation energies of these two defects behave oppositely under strain. As shown in Figure 3c, tensile strains reduce the formation energy of  $V_{\text{O}}^{\bullet\bullet}$  but increase the formation energies for  $V_{\text{Fe}}^{\bullet\bullet}$ . Assuming noninteracting defects as a first-order approximation, we estimate the strain dependency of the formation of the  $2V_{\text{Fe}}^{\bullet\bullet}-3V_{\text{O}}^{\bullet\bullet}$  Schottky defect (cf. eq 2) by a linear combination of the individual  $V_{\text{O}}^{\bullet\bullet}$  and  $V_{\text{Fe}}^{\bullet\bullet}$ . As a result, the formation energy of the  $2V_{\text{Fe}}^{\bullet\bullet}-3V_{\text{O}}^{\bullet\bullet}$  Schottky defect decreases under tensile strain; thus, tensile strain makes it easier to form and stabilize this type of defect that triggers exsolution of metal precipitates.

Figure 3d compares the relative change in the defect formation energy at the nominal strain values of the LSF/LSAT, LSF/STO, and LSF/KTO films. Here, the zero reference point corresponds to the unstrained state and negative  $\Delta E_f$  values indicate favorable defect formation. The formation energy of both  $V_{\text{O}}^{\bullet\bullet}$  and the  $2V_{\text{Fe}}^{\bullet\bullet}-3V_{\text{O}}^{\bullet\bullet}$  Schottky defect decreases from LSF/LSAT to LSF/STO and to LSF/

KTO. In other words, tensile strain could facilitate both the prereduction reaction (eq 1) and the Schottky reaction (eq 2), i.e., the two essential steps of exsolution in the LSF films. As a result, we would expect the tensile-strained LSF/KTO sample to exhibit the most enhanced exsolution among the three LSF samples.

To test this hypothesis, we compared the exsolution behavior of the three differently strained LSF thin films. Since LSF is expected to completely decompose over time in pure  $\text{H}_2$ , we did not focus on the equilibrated state of these films. Instead, we compared the surface chemistry and morphology of these films consistently after 0.5 h reduction in 0.5 mbar  $\text{H}_2$  at 400 °C. As shown in Supplementary Note 8, the as-prepared differently strained LSF films have similar surface cation chemistry and morphology. After Fe exsolution, a clear strain-dependent surface morphology and chemistry were observed on these samples (Figure 4). Consistent with our computational predictions, the tensile-strained LSF/KTO sample exhibited the most enhanced exsolution outcome. First, *in situ* Fe 3p spectra reflect an increase in the surface concentration of metallic iron [ $\text{Fe}^0$ ] from in-plane compression to tension (Figure 4a). Second, strain-dependent morphology was also observed on the same samples (Figure 4b). To better visualize the difference in the morphology, histograms of the equivalent disk radius as well as average height of these nanoparticles were generated from the images and are presented in Figure 4c,d. As illustrated, the mode value (Figure 4c) of the equivalent particle radius decreases from compressive to tensile strain: while the particles on the surface of LSF/LSAT have a mode radius of  $\sim 10$  nm, LSF/KTO generated finer particles with a mode radius of around 4 nm. Similar trends can also be observed for the average particle height (Figure 4d), which also decreases with the increase in the tensile strain.

Please note that due to the particle oxidation by the atmosphere (Figure 2), the *ex situ* atomic force microscopy (AFM) results shown in Figure 4 may overestimate the real particle size. In addition, due to the tip convolution effects,<sup>61</sup> the apparent topography in AFM scans can differ from the real particle morphology. In particular, the particles on the LSF/KTO surface are approaching the AFM resolution limit<sup>62</sup> (Supplementary Note 9). Nevertheless, by comparing the AFM resolution limit with the mode particle size and by examining the surface morphology with different AFM tips, we can safely exclude artifacts being responsible for the observed trends. As an additional support, we observed similar strain-dependent exsolution in LSF when reducing the thin-film samples in a UHV chamber at higher temperatures (Supplementary Note 10).

As summarized in Figure 4e, these findings clearly demonstrate that, even with the same bulk cation chemistry and the same reduction conditions, tuning point defect formation of LSF can significantly modulate its exsolution behavior. That is, we expect the tensile-strained LSF to have the highest surface  $\text{Fe}^0$  concentration, the largest particle density, as well as the finest particle size after exsolution. It should also be noted that, although the surface catalytic activity of these strained films was not examined in this work, this can be inferred from the previous work. First, it has been demonstrated that the surface catalytic activity of LSF increases with surface [ $\text{Fe}^0$ ] when LSF was used as a cathode for  $\text{H}_2\text{O}$  splitting.<sup>63</sup> Moreover, it is also known from other catalytic studies that smaller metal nanoparticles increase the

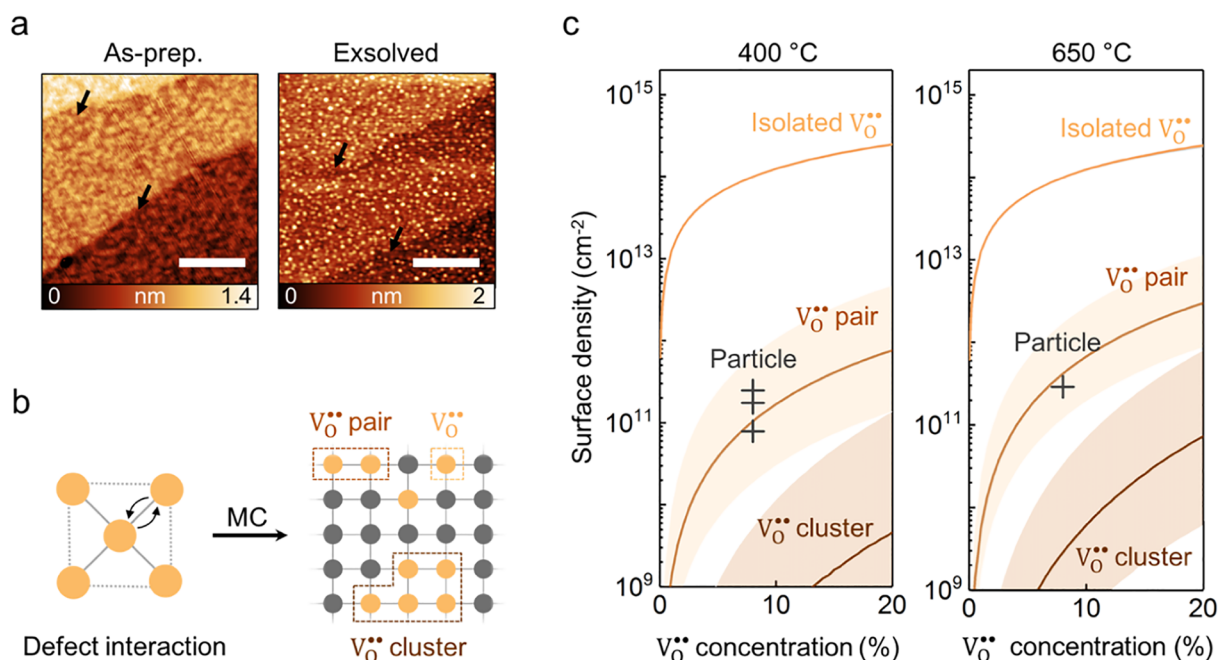


**Figure 5.** Correlation of  $Fe^0$  nanoparticle exsolution with  $V_O^{\bullet\bullet}$  pair formation. (a) AFM images of an atomically flat LSF(001) thin film before and after exsolution (same sample, different imaging spots). The arrows indicate the locations of the atomic steps. Scale bars: 200 nm. (b) Illustration of the defect model for the LSF(001) oxygen sublattice. The  $V_O^{\bullet\bullet}$  and  $O^{2-}$  sites are colored by orange and gray in the 2D cubic lattice, respectively. Two  $V_O^{\bullet\bullet}$  sites are considered to be in the same defect complex if they are nearest neighbors in a vacancy cluster. (c) Calculated surface densities of the isolated  $V_O^{\bullet\bullet}$ ,  $V_O^{\bullet\bullet}$  pairs, and  $V_O^{\bullet\bullet}$  clusters on the LSF(001) surface at 400 and 650 °C as a function of total  $V_O^{\bullet\bullet}$  concentration taken as a variable at the surface. The solid lines are obtained with a neighboring  $V_O^{\bullet\bullet}$ – $V_O^{\bullet\bullet}$  interaction energy of 0.3 eV, while the shaded region indicates the uncertainty in the defect modeling, which is calculated by changing the interaction energy by  $\pm 0.1$  eV. The scattered data points represent the experimentally observed iron particle density in Figures 4b and 5a. Note that the exsolved  $Fe^0$  nanoparticle densities fall well within the range of the computed surface  $V_O^{\bullet\bullet}$  pair density.

rate of various chemical reactions either by increasing the effective surface area per volume or by increasing the intrinsic reactivity of the catalyst material itself.<sup>2,19,64</sup> Therefore, with the highest  $[Fe^0]$  and smallest particle size on LSF/KTO, we anticipate the tensile-strained LSF to have the highest surface catalytic activity.

**Discussion on Strain Dependencies of Nanoparticle Exsolution.** Prior to this work, there have been conflicting reports regarding the dependence of exsolution on strain in perovskite oxides. For example, Kim et al.<sup>47</sup> reported tensile strain to promote Co exsolution in  $SrTi_{0.75}Co_{0.25}O_3$  (STC). On the contrary, Han et al.<sup>48</sup> reported that compressive strain facilitated Ni exsolution in  $La_{0.2}Sr_{0.7}Ti_{0.9}Ni_{0.1}O_3$  (LSTN). These studies suggest that the strain dependency can be system-dependent and the underlying mechanism still needs to be explored and discussed. As will be elaborated below, these seemingly contradictory observations can be reconciled within the framework proposed in this work in terms of point defect formation.

In the work by Kim et al.,<sup>47</sup> the authors interpret the strain dependence of exsolution based solely on the Co (B site) vacancy formation that becomes easier under tensile strain. Their analysis misses a key step in exsolution; that is, the reduction in the lattice itself. While Co vacancy formation is a part of the process, it is not the only, and certainly not the first, defect to be involved. Critically, one has to also consider the reduction of the metal cations in the oxide via oxygen vacancy formation. This is because B-site vacancies do not form independently in the host oxide during exsolution but rather form together with oxygen vacancies as Schottky defect. Moreover, a threshold of oxygen nonstoichiometry also needs

to be obtained in the lattice prior to the onset of exsolution. As a result, oxygen vacancy and Schottky defect should be the two fundamental point defects that determine the thermodynamics for exsolution, not the B-site vacancy alone. This point can be further supported by our observations for  $Fe^0$  exsolution in LSF: while the formation of Fe vacancy is more favorable under lattice compression (Figure 3c), the overall exsolution phenomenon was boosted with lattice tension (Figure 4 and Supplementary Note 10). As both Co vacancy and oxygen vacancy formation are easier in STC under tensile strain,<sup>47</sup> we can infer that tensile strain facilitates both the prereduction reaction (eq 1) and the Schottky reaction (eq 2) in STC, too. This explains the enhanced exsolution of Co on tensile-strained STC, similar to the LSF case reported in this work.

However, Han et al.'s work on LSTN, which shows more exsolution under compressive strain, does not explicitly consider the role of any point defects.<sup>48</sup> Nevertheless, we can estimate the strain dependency of point defects and the resulting exsolution in that material system, too, based on defect formation volume and strain energy. Since a point defect formation can result in lattice expansion or contraction,<sup>53</sup> the overall lattice volume often changes after the exsolution reaction (Supplementary Note 11). Conversely, the expanded/contracted lattice volume imposed facilitates or impedes the formation of point defects.<sup>56</sup> Thus, we expect that introducing tensile strain to the host oxide facilitates the formation of the defect(s) formed upon exsolution, if that oxide lattice expands after exsolution, and vice versa. For the case of LSF, lattice expands during exsolution (Figure 1e) so that applying a tensile strain to this material facilitates the formation of both oxygen vacancies and Schottky defects and results in more



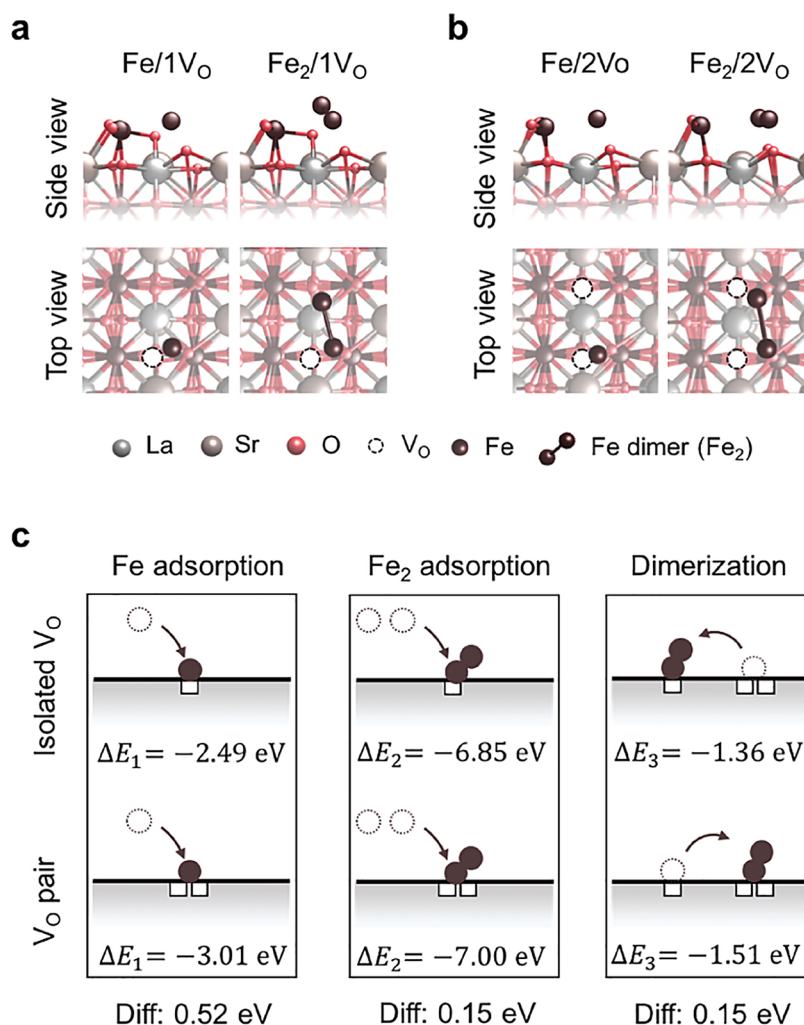


**Figure 6.** Effect of oxygen vacancy on adsorption of Fe atoms and Fe<sub>2</sub> dimers. (a and b) Fe and Fe<sub>2</sub> dimer structures on (a) isolated V<sub>O</sub><sup>••</sup> sites (1V<sub>O</sub>), and (b) V<sub>O</sub><sup>••</sup> pair (2V<sub>O</sub>) sites of the FeO<sub>2</sub>-terminated LSF(100) surface. (c) Comparison of the Fe adsorption, Fe<sub>2</sub> adsorption, and Fe dimerization energies on isolated V<sub>O</sub><sup>••</sup> and V<sub>O</sub><sup>••</sup> pairs. The energy differences (Diff.) for these two types of adsorption sites are summarized at the bottom of each panel. As illustrated, all three processes are more favored on V<sub>O</sub><sup>••</sup> pairs compared to on the isolated V<sub>O</sub><sup>••</sup>.

facile exsolution. However, the LSTN lattice contracted after Ni exsolution in Han's work,<sup>48</sup> indicating that the point defects involved in the exsolution reaction contract the lattice. Based on the above thoughts, we thus expect compressive strain to facilitate Ni exsolution in LSTN, which is consistent with the finding in ref 48.

Therefore, we can reconcile all these works, LSF in this report and LSTN and STC in refs 47 and 48, by considering the coupling of point defects involved in exsolution to the strain energy of the thin films. The favored strain tensor to promote nanoparticle exsolution in all the systems represent the one that favors the formation of the defects responsible for exsolution of metal particles out of the host oxide—in LSF, we have shown these defects to be oxygen vacancy and Schottky defects that are favored under tensile strain.

**V<sub>O</sub><sup>••</sup>-Mediated Nanoparticle Nucleation.** To date, several studies analyzed the nanoparticle exsolution based on the homogeneous nucleation theory.<sup>48,65</sup> In this section, we show that a heterogeneous nucleation model can be more appropriate to describe exsolution because nucleation of the metal particles can preferentially take place on defect sites at the surface. To do so, we investigated the morphological evolution of an atomically smooth LSF(001) thin film during

Fe<sup>0</sup> exsolution. The film was exsolved by thermal reduction in the UHV chamber (base pressure = 10<sup>−9</sup> mbar), where the Fe<sup>0</sup> exsolution was confirmed with *in situ* lab-based XPS. The *ex situ* AFM images of the LSF surfaces before and after exsolution are shown in Figure 5a. As illustrated, the as-prepared LSF thin film has flat terraces that are separated by monolayer atomic steps (Supplementary Note 12). After heating the LSF sample to 650 °C in UHV, nanoparticles started to form on the surface, together with the appearance of Fe<sup>0</sup> species in the Fe 2p photoelectron spectra (Supplementary Note 12). One important feature to note in Figure 5a is that the exsolved nanoparticles are uniformly distributed on the terraces, with no preference to the step edges. This characteristic suggests that certain defect sites at the surface are more favorable for nanoparticle nucleation and growth than step edges.<sup>27,28</sup>

As discussed in the Introduction section, we hypothesize that this preferential nucleation site is related to the surface oxygen vacancies. This is because both isolated and clustered V<sub>O</sub><sup>••</sup> sites have been shown as favorable nucleation sites for metal particle growth on binary oxides.<sup>66–68</sup> We cannot visually probe the nucleation sites on the LSF surface at the exsolution onset. We can, instead, correlate the concentration

of oxygen vacancies to the concentration of Fe<sup>0</sup> nanoparticles as an indirect measure to test this hypothesis. Since the exsolved particles are anchored and maintain their nucleation position,<sup>9</sup> we expect that the observed particle density largely reflects the density of the nucleation sites at the exsolution onset. Hence, a direct comparison between the Fe<sup>0</sup> nanoparticle density and the surface concentration of different types of defect structures can be useful in identifying the nature of the nucleation center.

Motivated by this idea, we combined DFT and MC simulations to model the microscopic defect structure of the LSF surface. The defect model takes into account the stability of both individual oxygen vacancies and their interacting pairs (clusters), as schematically shown in Figure 5c. First, we construct a 2D cubic lattice with periodic boundary conditions to represent the LSF(001) surface as experimentally observed (Supplementary Note 12). In this simulated 2D lattice, each element represents either a surface oxygen atom or a V<sub>O</sub><sup>••</sup>. Then, a model Metropolis MC simulation was conducted on this 2D lattice to simulate the process of defect clustering. The simulation temperatures were set to match the experimental exsolution condition in Figures 4 and 5. The interaction energy between the first nearest neighbor (1NN) V<sub>O</sub><sup>••</sup> sites is 0.3 ± 0.1 eV, with positive value representing repulsion. This interaction energy comes from our DFT calculations of vacancy–vacancy interactions on the FeO<sub>2</sub>-terminated LSF(001) surface. Finally, the concentrations of isolated V<sub>O</sub><sup>••</sup>, nearest-neighbor V<sub>O</sub><sup>••</sup> pairs, and V<sub>O</sub><sup>••</sup> clusters were calculated from the thermodynamically equilibrated lattices. Here, we define V<sub>O</sub><sup>••</sup> clusters as any V<sub>O</sub><sup>••</sup> complexes that contain more than two oxygen vacancies.

Figure 5c shows the surface density of the isolated V<sub>O</sub><sup>••</sup>, V<sub>O</sub><sup>••</sup> pairs, and V<sub>O</sub><sup>••</sup> clusters on the equilibrated oxygen sublattice as a function of surface oxygen deficiencies (V<sub>O</sub><sup>••</sup> concentration) at 400 and 650 °C. As illustrated, due to the V<sub>O</sub><sup>••</sup>–V<sub>O</sub><sup>••</sup> repulsion, the surface defect density follows isolated V<sub>O</sub><sup>••</sup> ≫ V<sub>O</sub><sup>••</sup> pairs ≫ V<sub>O</sub><sup>••</sup> clusters for both temperatures. Meanwhile, due to the increased thermal energy (*k<sub>B</sub>T*), the equilibrated V<sub>O</sub><sup>••</sup> pairs and V<sub>O</sub><sup>••</sup> clusters are higher at 650 °C than at 400 °C. In the same plot, the nanoparticle densities on the exsolved LSF surfaces (Figures 4b and 5a) are plotted at [V<sub>O</sub><sup>••</sup>] = 8%, the critical oxygen nonstoichiometry prior to the exsolution onset (Supplementary Note 3). By comparing the surface density of the exsolved Fe<sup>0</sup> nanoparticle and that of the V<sub>O</sub><sup>••</sup>-related point defects, we found that the measured particle density falls well within the range of the calculated V<sub>O</sub><sup>••</sup> pair concentration. However, the calculated density of both the individual V<sub>O</sub><sup>••</sup> sites and the large V<sub>O</sub><sup>••</sup> clusters are around 3 orders of magnitude off compared to the particle density. This comparison delivers a strong evidence that V<sub>O</sub><sup>••</sup> pairs are more likely to be the nucleation site for Fe<sup>0</sup> nanoparticle exsolution on the LSF surface, rather than individual V<sub>O</sub><sup>••</sup> sites and large V<sub>O</sub><sup>••</sup> clusters.

To assess the validity of this correlation at the atomic level, we examine whether Fe prefers to nucleate on the V<sub>O</sub><sup>••</sup> pairs. Since metal dimer formation can constitute the first step in metal nanoparticle nucleation,<sup>69</sup> we calculated the Fe dimer formation on the FeO<sub>2</sub>-terminated LSF(001) surface using DFT. Figure 6a,b shows the configuration of the adsorbed Fe and Fe<sub>2</sub> dimers at isolated V<sub>O</sub><sup>••</sup> and V<sub>O</sub><sup>••</sup> pairs. Based on these configurations, we calculated three characteristic energies associated with Fe dimer (Fe<sub>2</sub>) formation: Fe adsorption energy Δ*E*<sub>1</sub>, Fe dimer adsorption energy Δ*E*<sub>2</sub>, and the Fe dimerization energy Δ*E*<sub>3</sub>. These energies are defined as follows:

$$\Delta E_1(S_{\text{LSF}}) = -E(\text{Fe}/S_{\text{LSF}}) + E(\text{Fe}) + E(S_{\text{LSF}}) \quad (4)$$

$$\Delta E_2(S_{\text{LSF}}) = -E(\text{Fe}_2/S_{\text{LSF}}) + 2 \times E(\text{Fe}) + E(S_{\text{LSF}}) \quad (5)$$

$$\Delta E_3(S_{\text{LSF}}) = -E(\text{Fe}_2/S_{\text{LSF}}) - E(S'_{\text{LSF}}) + E(\text{Fe}/S_{\text{LSF}}) + E(\text{Fe}/S'_{\text{LSF}}) \quad (6)$$

where *S*<sub>LSF</sub> and *S'*<sub>LSF</sub> indicate the different adsorption sites on the LSF surface, which can be either an isolated V<sub>O</sub><sup>••</sup> or a V<sub>O</sub><sup>••</sup> pair. Δ*E*<sub>1</sub> and Δ*E*<sub>2</sub> measure the capability to bind an Fe adatom and an Fe<sub>2</sub> dimer to a given site on the LSF surface. Meanwhile, the Fe dimerization energy Δ*E*<sub>3</sub> measures the stability of the adsorbed Fe<sub>2</sub> dimer on a given site with respect to two separate Fe adatoms that are bound to an isolated V<sub>O</sub><sup>••</sup> and a V<sub>O</sub><sup>••</sup> pair, respectively.

These three characteristic energies for the isolated V<sub>O</sub><sup>••</sup> and V<sub>O</sub><sup>••</sup> pairs, together with the energy difference between these two types of adsorption sites, are summarized in Figure 6c. As shown, Fe and Fe<sub>2</sub> adsorption are favored on the V<sub>O</sub><sup>••</sup> pairs by 0.52 and 0.15 eV. Based on the equilibrium of two-level systems, we expect more than 99% of the Fe adatoms and more than 80% of Fe<sub>2</sub> adsorbates to occupy the V<sub>O</sub><sup>••</sup> pairs instead of the isolated V<sub>O</sub><sup>••</sup> sites at the exsolution conditions (Supplementary Note 13). The DFT calculation thus confirms that V<sub>O</sub><sup>••</sup> pairs are more favorable to form Fe adatoms and Fe dimers on the LSF surface, compared to the isolated V<sub>O</sub><sup>••</sup> sites. As a result of these MC simulations and DFT calculations, we can anticipate that the V<sub>O</sub><sup>••</sup> pairs formed during the prereduction step to be a critical defect structure responsible for the nanoparticle nucleation in exsolution. Assuming noninteracting defects as a first-order approximation, we estimate the strain dependency of oxygen vacancy pair formation to be similar to that of individual V<sub>O</sub><sup>••</sup> (Figure 3). As a result, tensile strain should also facilitate the formation of oxygen vacancy pairs in LSF. As a support of this argument, we note that strain-enhanced oxygen vacancy pairing/ordering has also been observed in previous studies.<sup>36,38</sup>

While further studies are required to illustrate the detailed nucleation mechanism, some practical insights can be already extrapolated from this work. Prior observations have shown that grain boundaries<sup>8,70</sup> can act as preferential nucleation sites for the exsolved nanoparticles. It is reasonable that on polycrystalline specimens, grain boundaries act as nucleation sites for the exsolved nanoparticles.<sup>71</sup> However, for those grain-boundary-facilitated nucleation scenarios, the particle density is much smaller (~10<sup>9</sup> cm<sup>-2</sup>) compared to the ones in this work (~10<sup>11</sup> cm<sup>-2</sup>). Therefore, promoting point-defect-mediated nucleation may be even more important than engineering grain boundaries in the host oxide to enhance the exsolution process. As a result, we expect oxygen vacancy engineering to be an effective approach to tailor the particle density in nanoparticle exsolution.

## CONCLUSIONS

In summary, using lattice strain to tune the point defect formation in a model perovskite oxide system, we demonstrate the capability to tailor nanoparticle exsolution using elastic strain and point defect engineering. We quantitatively measured the fundamental role of oxygen vacancy and Schottky defect formation in both the thermodynamics and the nucleation kinetics of Fe<sup>0</sup> nanoparticle exsolution in epitaxial thin-film LSF. Tensile strain favors the formation of

these defects involved in exsolution and thereby increases the amount of  $\text{Fe}^0$  metal formation with higher density and smaller size of particles compared to that on compressively strained films. Our experimental and computational results point to the oxygen vacancy pairs as the nucleation sites for the exsolved nanoparticles on the host oxide. The ability to engineer point defects in exsolution presents pathways for the design of nanostructured catalysts in energy and fuel conversion processes.

## METHODS

**Film Preparation.** The LSF target for pulsed laser deposition (PLD) was synthesized from powders prepared by the shake and bake method.  $\text{La}_2\text{O}_3$  (Sigma-Aldrich, 99.999%),  $\text{SrCO}_3$  (Sigma-Aldrich, 99.995%), and  $\text{Fe}_2\text{O}_3$  (Alfa Aesar, 99.998%) powders were mixed in appropriate ratios and ground using agate mortar and pestle for half an hour and then calcinated at 1000 °C for 5 h with a heating and cooling rate of 5 °C/min. The powders were then pressed into pellets using a hydrostatic press and sintered at 1350 °C for 20 h with a heating and cooling rate of 5 °C/min in stagnant air, thus yielding an LSF target. (001)-oriented  $10 \times 10 \times 0.5 \text{ mm}^3$  single crystal substrates (MTI Corporation, one side polished) were employed in this work. Each crystal substrate was cleaned in methanol (Koptech 200 Proof) in an ultrasonic bath for 3 min before the PLD deposition. The thin-film LSF was deposited with a KrF ( $\lambda = 248 \text{ nm}$ ) excimer laser, at a pulse repetition rate of 5 Hz and a laser energy of 400 mJ. During deposition, the substrate temperature was kept at 650 °C in an oxygen pressure of 20 mTorr. By applying 4000 laser pulses to the LSF target, an LSF thin film of about 20 nm thickness was grown on the substrate (substrate to target distance is 85 mm). After deposition, the sample was cooled in the deposition atmosphere at a cooling rate of 5 °C/min. The as-prepared PLD thin films were not exposed to any further surface treatment to avoid potential contamination. The deposited PLD thin films exhibited desired composition as revealed by ICP measurements (Supplementary Note 8).

**Near-Ambient Pressure X-ray Photoelectron Spectroscopy.** The NAP-XPS measurements were carried out at the NAP-XPS end station of the Pierre and Marie Curie University set on TEMPO beamline at Synchrotron SOLEIL and the IOS (23-ID-2) beamline of the National Synchrotron Light Source II (NSLS-II) at Brookhaven National Lab. The sample was placed on a ceramic heater, with thermocouples mounted directly onto the surface for temperature measurements. During the measurement, samples were preconditioned at 400 °C in 0.5 mbar  $\text{O}_2$  at the beginning of the measurement to remove adventitious carbon, cooled down in UHV, and then gradually heated up to 400 °C in 0.5 mbar flushing  $\text{H}_2$  to trigger Fe exsolution. At each temperature, samples were equilibrated for 20 min before the spectra collection.

**Atomic Force Microscopy and Reciprocal Space Mapping.** *Ex situ* AFM and RSM were performed on the LSF thin films after the NAP-XPS measurement. RSM was collected with a Bruker D8 high-resolution X-ray diffractometer using monochromatic  $\text{Cu K}\alpha_1$  radiation. To maximize the RSM signal from the film, an asymmetric configuration [103–] is employed for the measurement. AFM images were collected on a Cypher S AFM Microscope with tapping mode, using Bruker TESP-V2 AFM probe. Each of the AFM characterization was done on the center of the sample to avoid edge effects.

**Imaging and Elemental Mapping by STEM.** The LSF thin film for STEM imaging is grown on 0.5% Nb:STO(001) substrate to enhance sample electronic conductivity. Before characterization, the sample is reduced in 200 sccm 3%  $\text{H}_2/\text{N}_2$  at 650 °C for 5 h to trigger exsolution. The STEM specimen was prepared by conventional  $\text{Ga}^+$  focused ion beam (FIB) lift out procedure using a FIB-SEM (Helios Dual Beam 600). Prior to FIB work, a layer of carbon with 10 nm thickness was deposited on the LSF film by carbon evaporation with EMS QT150 ES. The FIB lamella was thinned using a final Ga ion accelerating voltage of 2 kV with the beam incident at  $\pm 1^\circ$ . The lamella was then polished using 600 eV Ar ions incident at  $\pm 10^\circ$

(Fischione Nanomill). STEM images were acquired using a probe-corrected JEOL ARM 200F operating at 200 kV, and images were calibrated to the substrate Nb:STO(001) lattice spacing of 3.905 nm. Elemental mapping was performed using EDX in the aforementioned STEM.

**Surface Defect Modeling.** A  $100 \times 100$  2D square lattice with periodic boundary conditions was employed to simulate the oxygen sublattice of the LSF(001) surface (Figure 5b). Since the aim of this simulation is to quantify oxygen vacancy cluster formation, the simulated lattice consists purely of oxygen and oxygen vacancy sites. In the simulated square 2D lattice, the interaction energy between the nearest  $\text{V}_\text{O}^\bullet$  sites was set to be 0.3 eV based on DFT calculation, while all other interactions were ignored. The Metropolis MC simulation was conducted as follows: First, 100 random configurations were generated as initial guesses at each  $[\text{V}_\text{O}^\bullet]$ . Then, each of the 100 initial lattices was evolved by switching sites according to the Metropolis scheme. Each MC step consisted of 10 000 switching trials, and the ensemble average was estimated by averaging 500 MCS after equilibrium. Finally, the densities of  $\text{V}_\text{O}^\bullet$ -related defects were calculated as the mean value of the 100 thermodynamically equilibrated lattices. In accord with the experiment, the simulation temperature was set to be 650 °C and the lattice constant for the 2D lattice was set to be 0.4 nm. A more detailed description of the MC simulation procedure is presented in ref 72.

**Density Functional Theory.** DFT calculations are performed with the Vienna *ab initio* Simulation Package (VASP) with PAW-PW91 pseudopotentials. Energy cut-off is set to 500 eV. A Hubbard U correction of 4.0 eV is applied to Fe. All calculations are spin-polarized. Defect formation energies in the bulk are calculated using a  $2 \times 2 \times 2 \text{ La}_{0.5}\text{Sr}_{0.5}\text{FeO}_3$  supercell (8 formula units) with the ordered alternating layers of La and Sr.<sup>73</sup> A  $4 \times 4 \times 4$  *k*-point grid is used. Multiple vacancy sites are considered and the configurations with the lowest energies are reported. Fe dimer formation calculations are performed on a  $2 \times 2$  BO-terminated LSF surface with 10 atomic layers (40 formula units) and 20 Å of vacuum. The five atomic layers in the middle are fixed during the structural relaxation to mimic bulk LSF. A  $2 \times 2 \times 1$  *k*-point grid is used. The atomic structures used in the DFT calculation are presented in Supplementary Note 7.

## ASSOCIATED CONTENT

### Supporting Information

The Supporting Information is available free of charge at <https://pubs.acs.org/doi/10.1021/acs.chemmater.1c00821>.

Details of the experimental and computational procedure, thermodynamic analysis of the exsolution condition, defect chemistry and diffusion characteristics of LSF, quantification of lattice strain, XPS and AFM analysis, and additional physical and chemical characterization (PDF)

## AUTHOR INFORMATION

### Corresponding Author

Bilge Yildiz – Department of Nuclear Science and Engineering and Department of Materials Science and Engineering, Massachusetts Institute of Technology, Cambridge, Massachusetts 02139, United States; [orcid.org/0000-0002-2688-5666](https://orcid.org/0000-0002-2688-5666); Email: [byildiz@mit.edu](mailto:byildiz@mit.edu)

### Authors

Jiayue Wang – Department of Nuclear Science and Engineering, Massachusetts Institute of Technology, Cambridge, Massachusetts 02139, United States; [orcid.org/0000-0002-2027-3634](https://orcid.org/0000-0002-2027-3634)

Jing Yang – Department of Materials Science and Engineering, Massachusetts Institute of Technology, Cambridge,



Massachusetts 02139, United States; [orcid.org/0000-0003-1855-0708](https://orcid.org/0000-0003-1855-0708)

**Alexander K. Opitz** – Department of Nuclear Science and Engineering, Massachusetts Institute of Technology, Cambridge, Massachusetts 02139, United States; Institute of Chemical Technologies and Analytics, TU Wien, 1060 Vienna, Austria; [orcid.org/0000-0002-2567-1885](https://orcid.org/0000-0002-2567-1885)

**William Bowman** – Department of Nuclear Science and Engineering, Massachusetts Institute of Technology, Cambridge, Massachusetts 02139, United States; [orcid.org/0000-0002-4346-1144](https://orcid.org/0000-0002-4346-1144)

**Roland Bliem** – Department of Nuclear Science and Engineering, Massachusetts Institute of Technology, Cambridge, Massachusetts 02139, United States; [orcid.org/0000-0002-8714-8942](https://orcid.org/0000-0002-8714-8942)

**Georgios Dimitrakopoulos** – Department of Nuclear Science and Engineering, Massachusetts Institute of Technology, Cambridge, Massachusetts 02139, United States; Department of Mechanical Engineering, Massachusetts Institute of Technology, Cambridge, Massachusetts 02139, United States; [orcid.org/0000-0001-6636-0517](https://orcid.org/0000-0001-6636-0517)

**Andreas Nenning** – Institute of Chemical Technologies and Analytics, TU Wien, 1060 Vienna, Austria

**Iradwikanari Waluyo** – National Synchrotron Light Source II, Brookhaven National Laboratory, Upton, New York 11973, United States; [orcid.org/0000-0002-4046-9722](https://orcid.org/0000-0002-4046-9722)

**Adrian Hunt** – National Synchrotron Light Source II, Brookhaven National Laboratory, Upton, New York 11973, United States

**Jean-Jacques Gallet** – Laboratoire de Chimie Physique Matière et Rayonnement – Campus Pierre et Marie Curie, Sorbonne Université, CNRS, F-75005 Paris, France; Synchrotron SOLEIL, L'Orme des Merisiers, Saint-Aubin F-91192, Gif-sur-Yvette, France

Complete contact information is available at:

<https://pubs.acs.org/10.1021/acs.chemmater.1c00821>

## Author Contributions

J.W., A.K.O., and B.Y. conceived the experiment design. J.W. prepared and characterized the samples. J.W., A.K.O., R.B., G.D., A.N., I.W., A.H., and J.-J.G. carried out the NAP-XPS experiments. J.Y. performed the DFT calculations and J.W. performed the MC simulations. W.B. conducted the STEM imaging. J.W. and B.Y. wrote the manuscript and all authors contributed to its revision. B.Y. supervised the project.

## Notes

The authors declare no competing financial interest.

## ACKNOWLEDGMENTS

The authors are grateful to the Exelon Corporation for the funding support. This research used the synchrotron radiation facilities at the National Synchrotron Light Source II (23-ID-2/IOS beamline), a U.S. Department of Energy (DOE) Office of Science User Facility operated for the DOE Office of Science by Brookhaven National Laboratory under contract no. DE-SC0012704, and the TEMPO beamline at the Synchrotron SOLEIL. This work was performed in part at the Center for Nanoscale Systems (CNS) at Harvard University, a member of the National Nanotechnology Coordinated Infrastructure Network (NNCI), which was supported by the National Science Foundation under NSF award no. 1541959. The authors acknowledge the facility

support from the Center for Materials Science and Engineering (NSF under award no. DMR-1419807) at MIT. The authors also thank the Photoemission End Stations (BL10B) in National Synchrotron Radiation Laboratory (NSRL) for the preliminary characterizations. J.W. and A.K.O. thank Christopher Herzig (TU Wien) for the assistance in the ICP measurements.

## REFERENCES

- (1) Munnik, P.; De Jongh, P. E.; De Jong, K. P. Recent Developments in the Synthesis of Supported Catalysts. *Chem. Rev.* **2015**, *115*, 6687–6718.
- (2) Liu, L.; Corma, A. Metal Catalysts for Heterogeneous Catalysis: From Single Atoms to Nanoclusters and Nanoparticles. *Chem. Rev.* **2018**, *118*, 4981–5079.
- (3) Van Deelen, T. W.; Hernández Mejía, C.; De Jong, K. P. Control of metal-support interactions in heterogeneous catalysts to enhance activity and selectivity. *Nat. Catal.* **2019**, *2*, 955–970.
- (4) Nishihata, Y.; Mizuki, J.; Akao, T.; Tanaka, H.; Uenishi, M.; Kimura, M.; Okamoto, T.; Hamada, N. Self-regeneration of a Pd-perovskite catalyst for automotive emissions control. *Nature* **2002**, *418*, 164–167.
- (5) Seshadri, R. Oxide Nanoparticles. *Chem. Nanomater.* **2004**, *94*–112.
- (6) Neagu, D.; Oh, T.-S.; Miller, D. N.; Ménard, H.; Bukhari, S. M.; Gamble, S. R.; Gorte, R. J.; Vohs, J. M.; Irvine, J. T. S. Nano-socketed nickel particles with enhanced coking resistance grown in situ by redox exsolution. *Nat. Commun.* **2015**, *6*, No. 8120.
- (7) Neagu, D.; Papaioannou, E. I.; Ramli, W. K. W.; Miller, D. N.; Murdoch, B. J.; Ménard, H.; Umar, A.; Barlow, A. J.; Cumpson, P. J.; Irvine, J. T. S.; Metcalfe, I. S. Demonstration of chemistry at a point through restructuring and catalytic activation at anchored nanoparticles. *Nat. Commun.* **2017**, *8*, No. 1855.
- (8) Jo, Y.-R.; Koo, B.; Seo, M. J.; Kim, J. K.; Lee, S.; Kim, K.; Han, J. W.; Jung, W.; Kim, B. J. Growth Kinetics of Individual Co Particles Ex-solved on SrTi<sub>0.75</sub>Co<sub>0.25</sub>O<sub>3-δ</sub> Polycrystalline Perovskite Thin Films. *J. Am. Chem. Soc.* **2019**, *141*, 6690–6697.
- (9) Neagu, D.; Kyriakou, V.; Roiban, I.-L.; Aouine, M.; Tang, C.; Caravaca, A.; Kousi, K.; Schreur-Piet, I.; Metcalfe, I. S.; Vernoux, P.; Van De Sanden, M. C. M.; Tsampas, M. N. In Situ Observation of Nanoparticle Exsolution from Perovskite Oxides: From Atomic Scale Mechanistic Insight to Nanostructure Tailoring. *ACS Nano* **2019**, *13*, 12996–13005.
- (10) Dai, S.; Zhang, S.; Katz, M. B.; Graham, G. W.; Pan, X. In Situ Observation of Rh-CaTiO<sub>3</sub> Catalysts during Reduction and Oxidation Treatments by Transmission Electron Microscopy. *ACS Catal.* **2017**, *7*, 1579–1582.
- (11) Lai, K.-Y.; Manthiram, A. Evolution of Exsolved Nanoparticles on a Perovskite Oxide Surface during a Redox Process. *Chem. Mater.* **2018**, *30*, 2838–2847.
- (12) Gao, Z.; Mogni, L. V.; Miller, E. C.; Railsback, J. G.; Barnett, S. A. A perspective on low-temperature solid oxide fuel cells. *Energy Environ. Sci.* **2016**, *9*, 1602–1644.
- (13) Zhu, T.; Troiani, H. E.; Mogni, L. V.; Han, M.; Barnett, S. A. Ni-Substituted Sr(Ti,Fe)O<sub>3</sub> SOFC Anodes: Achieving High Performance via Metal Alloy Nanoparticle Exsolution. *Joule* **2018**, *2*, 478–496.
- (14) Myung, J.-H.; Neagu, D.; Miller, D. N.; Irvine, J. T. S. Switching on electrocatalytic activity in solid oxide cells. *Nature* **2016**, *537*, 528–531.
- (15) Wu, X.-Y.; Ghoniem, A. F. Mixed ionic-electronic conducting (MIEC) membranes for thermochemical reduction of CO<sub>2</sub>: A review. *Prog. Energy Combust. Sci.* **2019**, *74*, 1–30.
- (16) Dimitrakopoulos, G.; Ghoniem, A. F.; Yildiz, B. In situ catalyst exsolution on perovskite oxides for the production of CO and synthesis gas in ceramic membrane reactors. *Sustainable Energy Fuels* **2019**, *3*, 2347–2355.

- (17) Kousi, K.; Neagu, D.; Bekris, L.; Papaioannou, E. I.; Metcalfe, I. S. Endogenous Nanoparticles Strain Perovskite Host Lattice Providing Oxygen Capacity and Driving Oxygen Exchange and CH<sub>4</sub> Conversion to Syngas. *Angew. Chem., Int. Ed.* **2020**, *59*, 2510–2519.
- (18) Sun, Y.-F.; Yang, Y.-L.; Chen, J.; Li, M.; Zhang, Y.-Q.; Li, J.-H.; Hua, B.; Luo, J.-L. Toward a rational photocatalyst design: A new formation strategy of co-catalyst/semiconductor heterostructures via in situ exsolution. *Chem. Commun.* **2018**, *54*, 1505–1508.
- (19) Haruta, M. Size- and support-dependency in the catalysis of gold. *Catal. Today* **1997**, *36*, 153–166.
- (20) Kobsiriphat, W.; Madsen, B. D.; Wang, Y.; Shah, M.; Marks, L. D.; Barnett, S. A. Nickel- and Ruthenium-Doped Lanthanum Chromite Anodes: Effects of Nanoscale Metal Precipitation on Solid Oxide Fuel Cell Performance. *J. Electrochem. Soc.* **2010**, *157*, B279–B284.
- (21) Wang, Y.; Liu, T.; Li, M.; Xia, C.; Zhou, B.; Chen, F. Exsolved Fe–Ni nano-particles from Sr<sub>2</sub>Fe<sub>1.3</sub>Ni<sub>0.2</sub>Mo<sub>0.5</sub>O<sub>6</sub> perovskite oxide as a cathode for solid oxide steam electrolysis cells. *J. Mater. Chem. A* **2016**, *4*, 14163–14169.
- (22) Götsch, T.; Köpfle, N.; Grünbacher, M.; Bernardi, J.; Carbonio, E. A.; Hävecker, M.; Knop-Gericke, A.; Bekheet, M. F.; Schlicker, L.; Doran, A.; Gurlo, A.; Franz, A.; Klötzer, B.; Penner, S. Crystallographic and electronic evolution of lanthanum strontium ferrite (La<sub>0.6</sub>Sr<sub>0.4</sub>FeO<sub>3-δ</sub>) thin film and bulk model systems during iron exsolution. *Phys. Chem. Chem. Phys.* **2019**, *21*, 3781–3794.
- (23) Kwon, O.; Sengodan, S.; Kim, K.; Kim, G.; Jeong, H. Y.; Shin, J.; Ju, Y.-W.; Han, J. W.; Kim, G. Exsolution trends and co-segregation aspects of self-grown catalyst nanoparticles in perovskites. *Nat. Commun.* **2017**, *8*, No. 15967.
- (24) Raman, A. S.; Vojvodic, A. Modeling Exsolution of Pt from ATiO<sub>3</sub> Perovskites (A = Ca/Sr/Ba) Using First-Principles Methods. *Chem. Mater.* **2020**, *32*, 9642–9649.
- (25) Neagu, D.; Tsekouras, G.; Miller, D. N.; Ménard, H.; Irvine, J. T. S. In situ growth of nanoparticles through control of non-stoichiometry. *Nat. Chem.* **2013**, *5*, 916–923.
- (26) Sun, Y.-F.; Zhang, Y.-Q.; Chen, J.; Li, J.-H.; Zhu, Y.-T.; Zeng, Y.-M.; Amirkhiz, B. S.; Li, J.; Hua, B.; Luo, J.-L. New Opportunity for In Situ Exsolution of Metallic Nanoparticles on Perovskite Parent. *Nano Lett.* **2016**, *16*, 5303–5309.
- (27) Bäumer, M.; Frank, M.; Heemeier, M.; Kühnemuth, R.; Stempel, S.; Freund, H.-J. Nucleation and growth of transition metals on a thin alumina film. *Surf. Sci.* **2000**, *454–456*, 957–962.
- (28) Haas, G.; Menck, A.; Brune, H.; Barth, J. V.; Venables, J. A.; Kern, K. Nucleation and growth of supported clusters at defect sites: Pd/MgO(001). *Phys. Rev. B* **2000**, *61*, 11105–11108.
- (29) Thanh, N. T. K.; Maclean, N.; Mahiddine, S. Mechanisms of Nucleation and Growth of Nanoparticles in Solution. *Chem. Rev.* **2014**, *114*, 7610–7630.
- (30) Yanagisawa, S.; Uozumi, A.; Hamada, I.; Morikawa, Y. Search for a Self-Regenerating Perovskite Catalyst Using Ab Initio Thermodynamics Calculations. *J. Phys. Chem. C* **2013**, *117*, 1278–1286.
- (31) Tanaka, H.; Taniguchi, M.; Uenishi, M.; Kajita, N.; Tan, I.; Nishihata, Y.; Mizuki, J.; Narita, K.; Kimura, M.; Kaneko, K. Self-Regenerating Rh- and Pt-Based Perovskite Catalysts for Automotive-Emissions Control. *Angew. Chem., Int. Ed.* **2006**, *45*, 5998–6002.
- (32) Hamada, I.; Uozumi, A.; Morikawa, Y.; Yanase, A.; Katayama-Yoshida, H. A Density Functional Theory Study of Self-Regenerating Catalysts LaFe<sub>1-x</sub>M<sub>x</sub>O<sub>3-y</sub> (M = Pd, Rh, Pt). *J. Am. Chem. Soc.* **2011**, *133*, 18506–18509.
- (33) Tian, Z.; Uozumi, A.; Hamada, I.; Yanagisawa, S.; Kizaki, H.; Inagaki, K.; Morikawa, Y. First-principles investigation on the segregation of Pd at LaFe<sub>1-x</sub>Pd<sub>x</sub>O<sub>3-y</sub> surfaces. *Nanoscale Res. Lett.* **2013**, *8*, 1–7.
- (34) Gao, Y.; Lu, Z.; You, T. L.; Wang, J.; Xie, L.; He, J.; Ciucci, F. Energetics of Nanoparticle Exsolution from Perovskite Oxides. *J. Phys. Chem. Lett.* **2018**, *9*, 3772–3778.
- (35) Kushima, A.; Yip, S.; Yildiz, B. Competing strain effects in reactivity of LaCoO<sub>3</sub> with oxygen. *Phys. Rev. B* **2010**, *82*, No. 115435.
- (36) Aschauer, U.; Pfenninger, R.; Selbach, S. M.; Grande, T.; Spaldin, N. A. Strain-controlled oxygen vacancy formation and ordering in CaMnO<sub>3</sub>. *Phys. Rev. B* **2013**, *88*, No. 054111.
- (37) Kushima, A.; Yildiz, B. Oxygen ion diffusivity in strained yttria stabilized zirconia: Where is the fastest strain? *J. Mater. Chem.* **2010**, *20*, 4809–4819.
- (38) Gazquez, J.; Bose, S.; Sharma, M.; Torija, M. A.; Pennycook, S. J.; Leighton, C.; Varela, M. Lattice mismatch accommodation via oxygen vacancy ordering in epitaxial La<sub>0.5</sub>Sr<sub>0.5</sub>CoO<sub>3-δ</sub> thin films. *APL Mater.* **2013**, *1*, No. 012105.
- (39) Orikasa, Y.; Nakao, T.; Oishi, M.; Ina, T.; Mineshige, A.; Amezawa, K.; Arai, H.; Ogumi, Z.; Uchimoto, Y. Local structural analysis for oxide ion transport in La<sub>0.6</sub>Sr<sub>0.4</sub>FeO<sub>3-δ</sub> cathodes. *J. Mater. Chem.* **2011**, *21*, 14013–14019.
- (40) Kuhn, M.; Hashimoto, S.; Sato, K.; Yashiro, K.; Mizusaki, J. Oxygen nonstoichiometry, thermo-chemical stability and lattice expansion of La<sub>0.6</sub>Sr<sub>0.4</sub>FeO<sub>3-δ</sub>. *Solid State Ionics* **2011**, *195*, 7–15.
- (41) Thalinger, R.; Gocyla, M.; Heggen, M.; Klötzer, B.; Penner, S. Exsolution of Fe and SrO Nanorods and Nanoparticles from Lanthanum Strontium Ferrite La<sub>0.6</sub>Sr<sub>0.4</sub>FeO<sub>3-δ</sub> Materials by Hydrogen Reduction. *J. Phys. Chem. C* **2015**, *119*, 22050–22056.
- (42) Nanning, A.; Fleig, J. Electrochemical XPS investigation of metal exsolution on SOFC electrodes: Controlling the electrode oxygen partial pressure in ultra-high-vacuum. *Surf. Sci.* **2019**, *680*, 43–51.
- (43) Opitz, A. K.; Nanning, A.; Rameshan, C.; Rameshan, R.; Blume, R.; Hävecker, M.; Knop-Gericke, A.; Rupprechter, G.; Fleig, J.; Klötzer, B. Enhancing Electrochemical Water-Splitting Kinetics by Polarization-Driven Formation of Near-Surface Iron(0): An In Situ XPS Study on Perovskite-Type Electrodes. *Angew. Chem., Int. Ed.* **2014**, *127*, 2666–2670.
- (44) Opitz, A. K.; Nanning, A.; Vonk, V.; Volkov, S.; Bertram, F.; Summerer, H.; Schwarz, S.; Steiger-Thirsfeld, A.; Bernardi, J.; Stierle, A.; Fleig, J. Understanding electrochemical switchability of perovskite-type exsolution catalysts. *Nat. Commun.* **2020**, *11*, No. 4801.
- (45) Katz, M. B.; Graham, G. W.; Duan, Y.; Liu, H.; Adamo, C.; Schlom, D. G.; Pan, X. Self-Regeneration of Pd–aFeO<sub>3</sub> Catalysts: New Insight from Atomic-Resolution Electron Microscopy. *J. Am. Chem. Soc.* **2011**, *133*, 18090–18093.
- (46) Katz, M. B.; Zhang, S.; Duan, Y.; Wang, H.; Fang, M.; Zhang, K.; Li, B.; Graham, G. W.; Pan, X. Reversible precipitation/dissolution of precious-metal clusters in perovskite-based catalyst materials: Bulk versus surface re-dispersion. *J. Catal.* **2012**, *293*, 145–148.
- (47) Kim, K.; Koo, B.; Jo, Y. R.; Lee, S.; Kim, J. K.; Kim, B. J.; Jung, W.; Han, J. W. Control of transition metal–oxygen bond strength boosts the redox ex-solution in a perovskite oxide surface. *Energy Environ. Sci.* **2020**, *13*, 3404–3411.
- (48) Han, H.; Park, J.; Nam, S. Y.; Kim, K. J.; Choi, G. M.; Parkin, S. P.; Jang, H. M.; Irvine, J. T. S. Lattice strain-enhanced exsolution of nanoparticles in thin films. *Nat. Commun.* **2019**, *10*, No. 1471.
- (49) Gopal, C. B.; Gabaly, F. E.; McDaniel, A. H.; Chueh, W. C. Origin and Tunability of Unusually Large Surface Capacitance in Doped Cerium Oxide Studied by Ambient-Pressure X-Ray Photoelectron Spectroscopy. *Adv. Mater.* **2016**, *28*, 4692–4697.
- (50) Crumlin, E. J.; Mutoro, E.; Liu, Z.; Grass, M. H.; Biegalski, M. D.; Lee, Y.-L.; Morgan, D.; Christen, H. M.; Blumh, M.; Shao-Horn, Y. Surface strontium enrichment on highly active perovskites for oxygen electrocatalysis in solid oxide fuel cells. *Energy Environ. Sci.* **2012**, *5*, 6081–6088.
- (51) Opitz, A. K.; Rameshan, C.; Kubicek, M.; Rupp, G. M.; Nanning, A.; Götsch, T.; Blume, R.; Hävecker, M.; Knop-Gericke, A.; Rupprechter, G.; Klötzer, B.; Fleig, J. The Chemical Evolution of the La<sub>0.6</sub>Sr<sub>0.4</sub>CoO<sub>3-δ</sub> Surface Under SOFC Operating Conditions and Its Implications for Electrochemical Oxygen Exchange Activity. *Top. Catal.* **2018**, *61*, 2129–2141.
- (52) Tuller, H. L.; Bishop, S. R. Point Defects in Oxides: Tailoring Materials Through Defect Engineering. *Annu. Rev. Mater. Res.* **2011**, *41*, 369–398.

- (53) Marrocchelli, D.; Bishop, S. R.; Tuller, H. L.; Yildiz, B. Understanding Chemical Expansion in Non-Stoichiometric Oxides: Ceria and Zirconia Case Studies. *Adv. Funct. Mater.* **2012**, *22*, 1958–1965.
- (54) Götsch, T.; Schlicker, L.; Bekheet, M. F.; Doran, A.; Grünbacher, M.; Praty, C.; Tada, M.; Matsui, H.; Ishiguro, N.; Gurlo, A.; Klötzera, B.; Penner, S. Structural investigations of  $\text{La}_{0.6}\text{Sr}_{0.4}\text{FeO}_{3-\delta}$  under reducing conditions: Kinetic and thermodynamic limitations for phase transformations and iron exsolution phenomena. *RSC Adv.* **2018**, *8*, 3120–3131.
- (55) Mueller, D. N.; Machala, M. L.; Bluhm, H.; Chueh, W. C. Redox activity of surface oxygen anions in oxygen-deficient perovskite oxides during electrochemical reactions. *Nat. Commun.* **2015**, *6*, No. 6097.
- (56) Aschauer, U.; Vonrüti, N.; Spaldin, N. A. Effect of epitaxial strain on cation and anion vacancy formation in MnO. *Phys. Rev. B* **2015**, *92*, No. 054103.
- (57) Xia, L.; Tybell, T.; Selbach, S. M. Bi vacancy formation in  $\text{BiFeO}_3$  epitaxial thin films under compressive (001)-strain from first principles. *J. Mater. Chem. C* **2019**, *7*, 4870–4878.
- (58) Zhang, B.; Fan, M.; Li, L.; Jian, J.; Huang, J.; Wang, H.; Kalaswad, M.; Wang, H. Tunable magnetic anisotropy of self-assembled Fe nanostructures within a  $\text{La}_{0.5}\text{Sr}_{0.5}\text{FeO}_3$  matrix. *Appl. Phys. Lett.* **2018**, *112*, No. 013104.
- (59) Mohaddes-Ardabili, L.; Zheng, H.; Ogale, S. B.; Hannoyer, B.; Tian, W.; Wang, J.; Lofland, S. E.; Shinde, S. R.; Zhao, T.; Jia, Y.; Salamanca-Riba, L.; Schlom, D. G.; Wuttig, M.; Ramesh, R. Self-assembled single-crystal ferromagnetic iron nanowires formed by decomposition. *Nat. Mater.* **2004**, *3*, 533–538.
- (60) Götsch, T.; Köpfle, N.; Schlicker, L.; Carbonio, E. A.; Hävecker, M.; Knop-Gericke, A.; Schloegl, R.; Bekheet, M. F.; Gurlo, A.; Doran, A. Treading in the Limited Stability Regime of Lanthanum Strontium Ferrite—Reduction, Phase Change and Exsolution. *ECS Trans.* **2019**, *91*, 1771–1781.
- (61) Shen, J.; Zhang, D.; Zhang, F.-H.; Gan, Y. AFM tip-sample convolution effects for cylinder protrusions. *Appl. Surf. Sci.* **2017**, *422*, 482–491.
- (62) Gan, Y. Atomic and subnanometer resolution in ambient conditions by atomic force microscopy. *Surf. Sci. Rep.* **2009**, *64*, 99–121.
- (63) Opitz, A. K.; Nenning, A.; Kogler, S.; Rameshan, C.; Rameshan, R.; Blume, R.; Haevecker, M.; Knop-Gericke, A.; Rupprechter, G.; Kloetzer, B. Water Splitting on Model-Composite  $\text{La}_{0.6}\text{Sr}_{0.4}\text{FeO}_{3-\delta}$  (LSF) Electrodes in  $\text{H}_2/\text{H}_2\text{O}$  Atmosphere. *ECS Trans.* **2015**, *68*, 3333–3343.
- (64) Flytzani-Stephanopoulos, M.; Gates, B. C. Atomically Dispersed Supported Metal Catalysts. *Annu. Rev. Chem. Biomol. Eng.* **2012**, *3*, 545–574.
- (65) Kim, K. J.; Han, H.; Defferriere, T.; Yoon, D.; Na, S.; Kim, S. J.; Dayaghi, A. M.; Son, J.; Oh, T.-S.; Jang, H. M.; Choi, G. M. Facet-Dependent In Situ Growth of Nanoparticles in Epitaxial Thin Films: The Role of Interfacial Energy. *J. Am. Chem. Soc.* **2019**, *141*, 7509–7517.
- (66) Min, B. K.; Wallace, W. T.; Santra, A. K.; Goodman, D. W. Role of Defects in the Nucleation and Growth of Au Nanoclusters on  $\text{SiO}_2$  Thin Films. *J. Phys. Chem. B* **2004**, *108*, 16339–16343.
- (67) Wahlström, E.; Lopez, N.; Schaub, R.; Thøstrup, P.; Rønnau, A.; Africh, C.; Lægsgaard, E.; Nørskov, J. K.; Besenbacher, F. Bonding of Gold Nanoclusters to Oxygen Vacancies on Rutile  $\text{TiO}_2(110)$ . *Phys. Rev. Lett.* **2003**, *90*, No. 026101.
- (68) Zhang, C.; Michaelides, A.; King, D. A.; Jenkins, S. J. Anchoring Sites for Initial Au Nucleation on  $\text{CeO}_2\{111\}$ : O Vacancy versus Ce Vacancy. *J. Phys. Chem. C* **2009**, *113*, 6411–6417.
- (69) Giordano, L.; Di Valentin, C.; Goniakowski, J.; Pacchioni, G. Nucleation of Pd Dimers at Defect Sites of the  $\text{MgO}(100)$  Surface. *Phys. Rev. Lett.* **2004**, *92*, No. 096105.
- (70) Kwak, N. W.; Jeong, S. J.; Seo, H. G.; Lee, S.; Kim, Y.; Kim, J. K.; Byeon, P.; Chung, S.-Y.; Jung, W. In situ synthesis of supported metal nanocatalysts through heterogeneous doping. *Nat. Commun.* **2018**, *9*, No. 4829.
- (71) Cahn, J. W. The kinetics of grain boundary nucleated reactions. *Acta Metall.* **1956**, *4*, 449–459.
- (72) Wang, J.; Bishop, S. R.; Sun, L.; Lu, Q.; Vardar, G.; Bliem, R.; Tsvetkov, N.; Crumlin, E. J.; Gallet, J.-J.; Bournel, F.; Waluyo, L.; Yildiz, B. Threshold catalytic onset of carbon formation on  $\text{CeO}_2$  during  $\text{CO}_2$  electrolysis: Mechanism and inhibition. *J. Mater. Chem. A* **2019**, *7*, 15233–15243.
- (73) Maiti, D.; Daza, Y. A.; Yung, M. M.; Kuhn, J. N.; Bhethanabotla, V. R. Oxygen vacancy formation characteristics in the bulk and across different surface terminations of  $\text{La}_{(1-x)}\text{Sr}_x\text{Fe}_{(1-y)}\text{Co}_y\text{O}_{(3-\delta)}$  perovskite oxides for  $\text{CO}_2$  conversion. *J. Mater. Chem. A* **2016**, *4*, 5137–5148.